PCCP

ROYAL SOCIETY OF CHEMISTRY

COMMUNICATION

View Article Online
View Journal

Check for updates

Cite this: DOI: 10.1039/d5cp03862f

Received 6th October 2025,
Accepted 24th October 2025

DOI: 10.1039/d5cp03862f

rsc.li/pccp

# Pressure-induced coupling of hydrated 4,4′-bipyridine

Raúl Torres-Cadena, W. Lakna N. Dayaratne, Mijoon Lee and Adam Jaffe *

**Aromatic molecules undergo pressure-induced bond formation, creating new species with intriguing structural, chemical, and electronic properties. Here, diffraction measurements, vibrational and photoluminescence spectroscopies, and mass spectrometry suggest that hydrated 4,4′-bipyridine undergoes two distinct irreversible reactions upon compression: dimerization coupled to loss of hydrogen atoms and oligomerization without atom loss.**

Pressure can alter the physical and chemical properties of molecules and materials, revealing exotic behavior such as superconductivity,[1] superhardness,[2] and pressure-induced polymerization.[3] Pressure-induced bond formation has been explored in small organic molecules, with a focus on aromatic systems such as benzene,[4] pyridine,[5] pyridazine,[6] and azobenzene,[7] as well as unsaturated hydrocarbons including acetylene,[8] 1-hexene,[9] and butadiene.[10] While these molecules show the formation of oligomeric/polymeric species when compressed, the pressure at which such behavior occurs is affected by the molecular derivatives' composition, structure, and solid-state packing, resulting in a wide pressure range for reactivity from *ca.* 3.6 to 20 GPa. Examining such molecular species under pressure therefore provides valuable insight into the interplay of intermolecular interactions that arise in the solid state, mechanisms of uncommon bond formation, and the energy landscape in non-standard thermodynamic conditions. These studies can also produce new and complex oligomeric and polymeric compounds that are less synthetically accessible.

4,4′-Bipyridine (4,4′-bipy) (Fig. 1) is a versatile ditopic molecule featuring two aromatic nitrogen atoms possessing Lewis basic electron lone pairs capable of binding coordination centers. Although this molecule is relatively rigid, the pyridyl rings have some rotational freedom without disrupting the orientation of the lone pairs.[11] Given these structural features, 4,4′-bipy plays an important role as a ligand in metal–organic frameworks (MOFs),[12] coordination complexes,[11] and solid-state materials.[11,13] Determination of its response to high pressure is therefore of considerable interest for the molecular reactivity described above as well as to inform how these more complex solids evolve under compression. To our knowledge, molecular 4,4′-bipy has only been examined under compression to 7 GPa,[14] and no pressure-induced bond formation or polymerization has been reported. High-pressure studies on systems containing 4,4′-bipy as a ligand have also been conducted, such as in MOFs,[12] salts,[15] or cocrystals,[16,17] yet again without evidence of pressure-induced bond formation. Recently, however, we demonstrated that 4,4′-bipy-pillared hybrid metal oxides exhibit intriguing negative volume compressibility that appears to be driven by compression-induced formation of $sp^2$-hybridized C–C bonds.[18] Critically, this behavior is distinct from much of the reactivity described above for molecular solids under pressure—in which new C–C bonds are typically $sp^3$-hybridized—and is likely coupled to dehydrogenation that generates electron and proton equivalents that migrate to the metal oxide layer. To better understand its high-pressure reactivity and decouple the influence of a hybrid

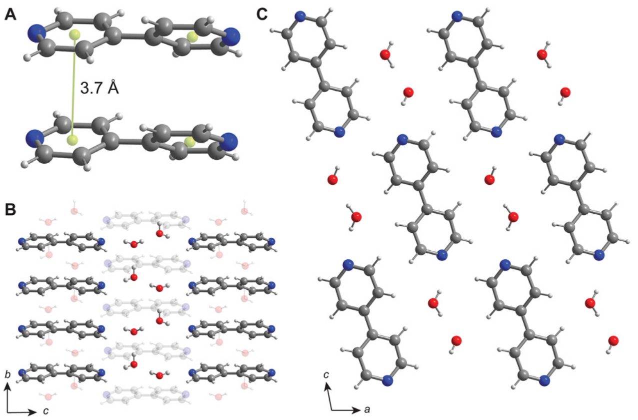

Fig. 1 Molecular packing of 4,4′-bipy·$H_2O$. (A) Intermolecular stacking and ring centroid–centroid distances. (B) Packing of 4,4′-bipy and water molecules along the *a* axis. A second layer beneath is indicated with transparency. (C) Molecular packing along the *b* axis. Gray, blue, red, and light gray spheres are C, N, O, and H atoms, respectively.

---

*Department of Chemistry and Biochemistry, University of Notre Dame, Notre Dame, Indiana 46556, USA. E-mail: ajaffe@nd.edu*

framework, here, we showcase the pressure-induced evolution of hydrated molecular 4,4′-bipy.

Hydrated 4,4′-bipy (4,4′-bipy·$H_2O$) crystallizes in the monoclinic space group $P2_1/c$. The unit cell contains two crystallographically unique 4,4′-bipy molecules and four water molecules.[19] The pyridyl rings are non-planar, exemplified by a dihedral angle about the connecting C–C bond of *ca.* 41° (Fig. 1A). However, a centroid–centroid distance of *ca.* 3.7 Å between adjacent pyridyl rings may allow for some weak π–π stacking (Fig. 1A).[19] Each nitrogen forms a hydrogen bond with a water molecule at a distance of *ca.* 2.1 Å (Fig. S1), which is in turn linked to another water molecule connected to the next 4,4′-bipy molecule, resulting in a continuous network that leads to the formation of a sheet-like arrangement (Fig. 1B, C and Fig. S1). The 4,4′-bipy and water molecules are arranged in a checkerboard-like pattern in the *ac* plane (Fig. 1C). We note the hydrated phase was selected rather than the anhydrous compound because the latter crystallizes in a lower-symmetry triclinic space group ($P\bar{1}$) with alternating molecular orientations, leading to a more complex packing motif than the monoclinic hydrated phase. The incorporation of structural water also provides a more polar, high-dielectric environment more similar to that within our previously reported hybrid metal oxides, thus facilitating clearer interpretation of the compression response.

To probe its pressure-dependent evolution, we subjected microcrystalline 4,4′-bipy·$H_2O$ to gigapascal-scale pressure in a diamond-anvil cell (DAC) featuring 300 μm culets. Raman spectra measured *in situ* show that all vibrational modes blueshift with increasing pressure, accompanied by peak broadening (Fig. 2A and Fig. S2, S3). The onset of a potential phase transition is observed upon compression past 5 GPa, characterized by the splitting of peaks such as those at *ca.* 644 $cm^{-1}$ and 755 $cm^{-1}$ (Fig. S3). We assign the first peak as an in-plane ring deformation and the second as a combination of ring breathing, C–N stretching, and C–C stretching vibrations.[14] A complete loss of Raman peaks is observed *ca.* 20 GPa, likely associated with decreased visible light penetration due to increased absorption and/or reflectivity. Indeed, the compound converts from pale yellow to dark brown/black (Fig. S4).

We explored the compression-induced structural evolution of 4,4′-bipy·$H_2O$ in greater detail up to approximately 41 GPa using synchrotron powder X-ray diffraction (PXRD). Consistent with our vibrational analysis, upon compression past 6 GPa, an apparent first-order phase transition is observed, though its onset may begin at lower pressure. Here, a new diffraction peak is observed at 7° 2$\theta$ coupled with the onset of potential peak splitting behavior *ca.* 11° and 12° 2$\theta$—behavior that becomes even more apparent at higher pressure (Fig. 2B and Fig. S5). These features are assigned to the (200) and (30$\bar{3}$) reflections of the ambient-pressure phase, respectively (Table S1). All peaks then continue to shift to higher 2$\theta$ values with compression up to *ca.* 22 GPa, at which point some reflections disappear with only those assigned as (101), (200), (021), and (022) remaining, thus aligning well with the behavior observed by Raman spectroscopy. Increased background scatter is also observed that may indicate partial amorphization/disorder. Upon decompression, only the (101) and (200) reflections persist. Le Bail refinements indicate a continuous decrease in unit cell volume upon increasing pressure (Fig. 2C). Interestingly, the structure appears to be more compressible along the *a* and *b* lattice parameters than along *c* (Fig. S6). The *a* axis features 4,4′-bipy molecules packed adjacent to water molecules where no strong hydrogen bonding is apparent, while the *b* axis corresponds to the direction of stacking for the aromatic 4,4′-bipy molecules. This lack of strong intermolecular interactions along *a* and *b* may explain their relatively high compressibility. On the other hand, the *c* axis may be less compressible due to the presence of stronger hydrogen bonding chains. Fitting the unit cell volume as a function of pressure to the Birch–Murnaghan equation of state corroborates a phase transition above *ca.* 7 GPa, indicating an increase in ambient-pressure bulk modulus ($K_0$) from 13(1) GPa to 26(5) GPa (Fig. S7). We note, however, that the foregoing Le Bail analysis only provides information on crystalline material featuring long-range order and does not provide insight into the behavior of any amorphous/disordered components.

To gain better insight into the hypothesized pressure-induced reactivity of 4,4′-bipy, we performed bulk compression to 17 GPa using a Paris-Edinburgh (PE) pressure cell. Based on

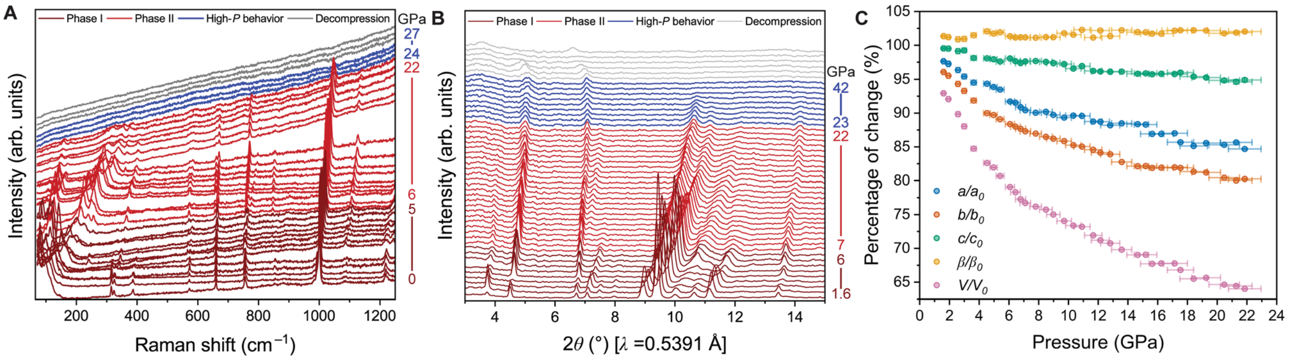

Fig. 2 Evolution of 4,4′-bipy·$H_2O$ under pressure. (A) Raman spectra upon compression to 27 GPa and decompression to ambient pressure with KBr as pressure medium to better-resolve peaks. (B) Powder X-ray diffraction patterns during compression to 42 GPa and decompression to ambient pressure. (C) Lattice constant and unit cell volume evolution derived from Le Bail refinement.

our *in situ* measurements, this pressure—the maximum achievable value within the cell—is not sufficient to fully convert the sample to its highest-pressure state, instead yielding a partially converted sample. We note that any post-compression analysis therefore also contains a significant fraction of starting material, whose compression-induced behavior appears to be at least partially reversible below *ca.* 22 GPa. Indeed, an *ex situ* PXRD pattern of the sample treated in the PE cell shows the presence of 4,4′-bipy·$H_2O$ along with a peak disappearing at 13.6° 2$\theta$ corresponding to (010) reflection (Fig. S8). The loss and/or broadening of peaks again suggests partial amorphization/disorder within the product. Raman spectra for post-compression sample show the loss of a peak *ca.* 2900 $cm^{-1}$ and the appearance of a peak at 1400 $cm^{-1}$ corresponding to a likely ring deformation (Fig. S9). IR spectra of the pre- and post-compression sample show no significant differences (Fig. S10). This is expected if the bulk of the sample consists of mainly unreacted monomers.

We performed liquid chromatography-mass spectrometry (LC-MS) for the pre- and post-compression samples (Fig. 3A, B and Fig. S11). As expected, a peak is observed at 157.1 *m*/*z* (mass to charge ratio), consistent with a 4,4′-bipy molecule (156 amu) singly protonated in the instrument's positive ion mode. After compression we observe a unique 311.1 *m*/*z* feature at a retention time of 8.2 min. A dimer resulting from a single C–C bond formation *via* dearomatization and formation of $sp^3$ centers would have a mass of 312 amu, yielding a peak at 313 *m*/*z* after instrument protonation. The presence of a peak at 311 *m*/*z* indicates dimer formation coupled with dehydrogenation (loss of two H atoms)—similar behavior to that which we have observed in 4,4′-bipy-templated hybrid metal oxides.[18] We also performed matrix-assisted laser desorption ionization (MALDI) mass spectrometry on the compressed sample (Fig. 3C and S12). We again observe a monomeric peak at 157.1 *m*/*z*, as well as at 311.1 *m*/*z*, corroborating the formation of a dimer species accompanied by the loss of two H atoms. We then observe peaks at higher *m*/*z* separated by a consistent mass difference of 156 amu—features only observed in post-compression 4,4′-bipy·$H_2O$. We note that such oligomers may not be observed *via* LC-MS if they do not pass through the column. Additionally, the possibility of these signals arising from MALDI-induced cluster ion formation between the dimer and additional monomers cannot be fully ruled out. Nevertheless, this apparent oligomerization exclusively observed post-compression may suggest that distinct higher-order oligomeric/polymeric species are formed under pressure without dehydrogenation (see SI for additional discussion). Interestingly, in addition to the main oligomeric series, a secondary series of oligomeric peaks is observed, shifted positively by 16 amu, consistent with potential oxidation of the products—such as through reaction with nearby water molecules or molecular oxygen.

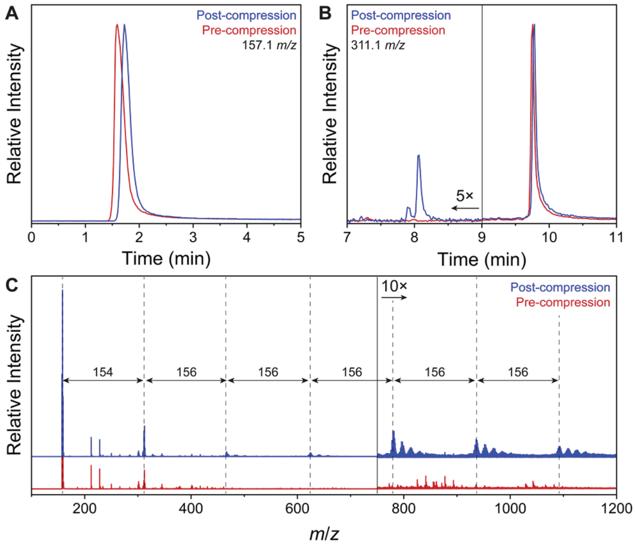

**Fig. 3** Analysis of pre- and post-compression 4,4′-bipy·$H_2O$. LC-MS extracted-ion chromatograms at (A) 157.1 *m*/*z* and (B) 311.1 *m*/*z*. The 311.1 *m*/*z* peak observed at 9.8 min in all samples is attributed either to a separate molecular dimer formed *in situ* within the instrument or a sample contaminant. (C) MALDI traces.

We then investigated the optical and electronic effects of pressure on the 4,4′-bipy·$H_2O$ system. *In situ* photoluminescence measurements using a 405 nm excitation exhibit an overall decrease in photoluminescence intensity with increasing pressure up to 17 GPa, prior to its complete disappearance above 17 GPa (Fig. 4). However, three distinct regimes of behavior are observed. At lower pressure, from ambient pressure to 5 GPa, a redshift of the photoluminescence peak centered at 2.51 eV occurs, shifting to *ca.* 2.47 eV (Fig. 4A). Such behavior has been previously attributed to pressure-induced structural planarization leading to enhanced molecular interactions such as π–π stacking.[20] In agreement with our Raman and PXRD results, a change is then observed from 5 to 11 GPa (Fig. 4B), wherein a new peak at 2.8 eV grows in intensity with increasing pressure. Further compression shows the same peak decreasing in intensity and eventually disappearing above 17 GPa (Fig. S13), thereby tracking with the disappearance of Raman signals and apparent partial amorphization observed in the PXRD data. *Ex situ* UV-visible diffuse reflectance spectroscopy on pre- and post-compression samples shows a new feature appearing at approximately 3 eV (Fig. S14). Taken together, these newly observed optical features may therefore

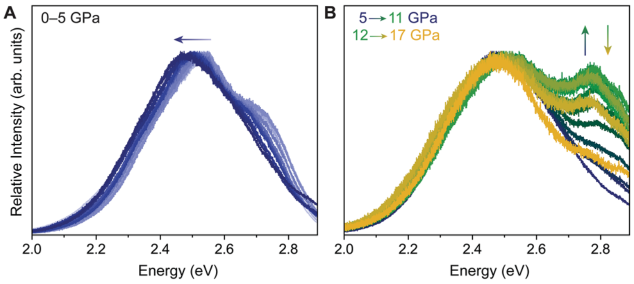

**Fig. 4** Normalized photoluminescence spectral evolution upon compression for 4,4′-bipy·$H_2O$. (A) 0–5 GPa (light blue to dark blue) and (B) 5–11 GPa (dark blue to green) and 12–17 GPa (green to yellow).

relate to newly formed dimers and/or oligomers. No electron paramagnetic resonance signal was observed in either pre-compression samples or post-compression material that was handled under air-free conditions (Fig. S15), suggesting the absence of stable radical species in the recovered sample after compression. However, we cannot rule out the mechanistic possibility that radical species evolve during compression-induced reactivity.

We note that upon compression of 4,4′-bipy·$H_2O$, the metal gasket in pressure cells appears to expand (Fig. S4). To confirm this effect—and to better observe optical changes under pressure—we measured the high-pressure behavior of 4,4′-bipy·$H_2O$ both with and without a KBr pressure medium. The gasket expansion was especially pronounced in the latter. The mechanism behind this macroscopic behavior is unknown, yet intriguing, and could relate to the strong newly formed bonds. This will be the subject of further investigation. Further, the role of the water molecules in structural evolution during compression remains to be fully elucidated and future studies on anhydrous 4,4′-bipy under pressure could provide valuable complementary insight into the present work.

## Conclusions

Based on these collective results, we propose that two pressure-induced C–C bond formation mechanisms occur in 4,4′-bipy·$H_2O$: (1) dimerization coupled to dehydrogenation, thereby retaining $sp^2$ hybridization of carbon centers, and (2) oligomerization without hydrogen loss, leading to the formation of $sp^3$ carbon centers. The dimerization process is similar to what is observed in the hybrid $(4,4'\text{-bipy})_{0.5}MoO_3$ system,[18] though this behavior appears more facile in the hybrid, with a lower reaction onset pressure and a greater degree of bond formation when compressed to the maximum pressure in a PE cell. Meanwhile, the oligomerization process may be similar to what is observed for benzene and pyridine, where evidence suggests the formation of $sp^3$-hybridized nanothreads.[5,21,22] Taken together, we hypothesize that the dehydrogenative dimerization in the compressed 4,4′-bipy·$H_2O$ may be facilitated by molecular planarization and/or decreased π–π distances. However, the fate of the evolved hydrogen in this process is unknown and requires further investigation. Oligomerization without H atom loss is then likely enabled by the relatively numerous degrees of freedom in the molecular solid. On the other hand, the comparatively enhanced dimerization—and even minor $sp^2$-hybridized trimerization—in the hybrid metal oxide[18] may therefore be explained by the enforced proximity of 4,4′-bipy molecules in the hybrid architecture and the presence of metal oxide layers that can accept protons and electrons. The absence of $sp^3$-hybridized oligomerization in the hybrid may result from an inability of the confined molecular species to undergo major structural rearrangement. Overall, the foregoing results suggest exciting design principles for the control of pressure-induced bond formation in molecular and extended solids.

## Conflicts of interest

There are no conflicts to declare.

## Data availability

The data supporting this article have been included as part of the supplementary information (SI). Supplementary information: experimental details, diffraction patterns, spectra, and supplemental discussion. See DOI: https://doi.org/10.1039/d5cp03862f.

## Acknowledgements

This material is based upon work supported by the National Science Foundation (NSF) under Award No. DMR-2338086. Synchrotron X-ray diffraction studies were performed at Beamline 12.2.2 at the Advanced Light Source (ALS) at Lawrence Berkeley National Laboratory. The ALS is supported by the Director, Office of Science, Office of Basic Energy Sciences, of the U.S. Department of Energy under Contract No. DE-AC02-05CH11232. The high-pressure facilities at the ALS are supported by COMPRES, the Consortium for Material Properties Research in Earth Science under NSD Cooperative Agreement EAR 11-57758. We gratefully acknowledge Dr Martin Kunz and Dr Bora Kalkan for assistance with XRD studies at the ALS. PE compression synthesis was carried out at the Spallation Neutron Source, a DOE Office of Science User Facility operated by the Oak Ridge National Laboratory. The offline pressure synthesis was performed at Spallation Neutron and Pressure (SNAP). We acknowledge Jamie Molaison and Dr Chris Ridley for their assistance with the PE synthesis. LC-MS and MALDI measurements were collected using instruments at the Notre Dame Mass Spectrometry & Proteomics Facility (MSPF). The MALDI TOF mass spectrometer is supported by the NSF MRI grant under Award No. CHE-1625944. The Impact II mass spectrometer is supported by the Equipment Purchase, Restoration and Renewal Program Notre Dame Research. We thank Dr William Boggess for his assistance in mass spectrometry experimentation and data analysis. We thank the ND Energy Materials Characterization Facility (MCF) for the use of the UV-visible spectrometer to acquire diffuse reflectance measurements. The MCF is supported by Notre Dame Research. Electron paramagnetic resonance studies were carried out at the Notre Dame Magnetic Resonance Research Center (MRRC). We thank Prof. Prashant Kamat for the use of the fluorimeter used to collect excitation spectra.

## Notes and references

1 A. P. Drozdov, P. P. Kong, V. S. Minkov, S. P. Besedin, M. A. Kuzovnikov, S. Mozaffari, L. Balicas, F. F. Balakirev, D. E. Graf, V. B. Prakapenka, E. Greenberg, D. A. Knyazev, M. Tkacz and M. I. Eremets, *Nature*, 2019, **569**, 528–531.
2 W. L. Mao, H.-k Mao, P. J. Eng, T. P. Trainor, M. Newville, C.-c Kao, D. L. Heinz, J. Shu, Y. Meng and R. J. Hemley, *Science*, 2003, **302**, 425–427.

3 F. Li, J. Xu, Y. Wang, H. Zheng and K. Li, *Molecules*, 2021, **26**, 7581.
4 P. Pruzan, J. C. Chervin, M. M. Thiéry, J. P. Itié, J. M. Besson, J. P. Forgerit and M. Revault, *J. Chem. Phys.*, 1990, **92**, 6910–6915.
5 X. Li, T. Wang, P. Duan, M. Baldini, H.-T. Huang, B. Chen, S. J. Juhl, D. Koeplinger, V. H. Crespi, K. Schmidt-Rohr, R. Hoffmann, N. Alem, M. Guthrie, X. Zhang and J. V. Badding, *J. Am. Chem. Soc.*, 2018, **140**, 4969–4972.
6 S. G. Dunning, L. Zhu, B. Chen, S. Chariton, V. B. Prakapenka, M. Somayazulu and T. A. Strobel, *J. Am. Chem. Soc.*, 2022, **144**, 2073–2078.
7 P. Zhang, D. Gao, X. Tang, X. Yang, H. Zheng, Y. Wang, X. Wang, J. Xu, Z. Wang, J. Liu, X. Wang, J. Ju, M. Tang, X. Dong, K. Li and H.-k. Mao, *J. Am. Chem. Soc.*, 2023, **145**, 6845–6852.
8 J. Sun, X. Dong, Y. Wang, K. Li, H. Zheng, L. Wang, G. D. Cody, C. A. Tulk, J. J. Molaison, X. Lin, Y. Meng, C. Jin and H.-k. Mao, *Angew. Chem., Int. Ed.*, 2017, **56**, 6553–6557.
9 J. Xu, P. Lang, S. Liang, J. Zhang, Y. Fei, Y. Wang, D. Gao, T. Hattori, J. Abe, X. Dong, H. Zheng and K. Li, *J. Phys. Chem. Lett.*, 2025, **16**, 2445–2451.
10 M. Citroni, M. Ceppatelli, R. Bini and V. Schettino, *Science*, 2002, **295**, 2058–2060.
11 K. Biradha, M. Sarkar and L. Rajput, *Chem. Commun.*, 2006, 4169–4179.
12 P. Pachfule, T. Panda, C. Dey and R. Banerjee, *CrystEngComm*, 2010, **12**, 2381–2389.
13 W. L. N. Dayaratne, R. Torres-Cadena, B. P. Schmitt, E. M. Westrick and A. Jaffe, *Chem. Sci.*, 2023, **14**, 10756–10767.
14 A. Li, P. Li, Y. Geng, S. Xu, H. Zhang, H. Cui and W. Xu, *Spectrochim. Acta, Part A*, 2018, **202**, 70–75.
15 M. Anioła and A. Katrusiak, *CrystEngComm*, 2016, **18**, 3223–3228.
16 I. L. Christopher, X. Liu, H. J. Lloyd, C. L. Bull, N. P. Funnell, P. Portius, A. A. L. Michalchuk, S. R. Kennedy, C. R. Pulham and C. A. Morrison, *Phys. Chem. Chem. Phys.*, 2024, **26**, 16859–16870.
17 E. Patyk-Kaźmierczak, F. Izquierdo-Ruiz, A. Lobato, M. Kaźmierczak, I. Moszczyńska, A. Olejniczak and J. M. Recio, *IUCrJ*, 2024, **11**, 168–181.
18 R. Torres-Cadena, W. L. N. Dayaratne, H.-T. Chen, E. L. Kovrigin, M. G. Tucker, B. Haberl and A. Jaffe, *J. Am. Chem. Soc.*, 2025, **147**, 25931–25939.
19 W. Ji, B. Xue, S. Bera, S. Guerin, Y. Liu, H. Yuan, Q. Li, C. Yuan, L. J. W. Shimon, Q. Ma, E. Kiely, S. A. M. Tofail, M. Si, X. Yan, Y. Cao, W. Wang, R. Yang, D. Thompson, J. Li and E. Gazit, *ACS Nano*, 2020, **14**, 10704–10715.
20 Q. Qi, J. Qian, X. Tan, J. Zhang, L. Wang, B. Xu, B. Zou and W. Tian, *Adv. Funct. Mater.*, 2015, **25**, 4005–4010.
21 B. Chen, R. Hoffmann, N. W. Ashcroft, J. Badding, E. Xu and V. Crespi, *J. Am. Chem. Soc.*, 2015, **137**, 14373–14386.
22 T. C. Fitzgibbons, M. Guthrie, E.-s. Xu, V. H. Crespi, S. K. Davidowski, G. D. Cody, N. Alem and J. V. Badding, *Nat. Mater.*, 2015, **14**, 43–47.